# An experimental and numerical investigation into damage mechanisms in tapered laminates under tensile loading

Bing Zhang[a,*], Luiz F. Kawashita[a], Mike I. Jones[a], James K. Lander[b], Stephen R. Hallett[a]

[a]Bristol Composites Institute (ACCIS), University of Bristol, Queen's Building, University Walk, Bristol BS8 1TR, UK

[b]Rolls-Royce Plc, Derby DE24 8BJ, UK

## Abstract

Through-thickness thickness reductions in laminated composites are essential for weight and aerodynamic efficiency, but they can also be the site of damage initiation. Tensile failure mechanisms of modestly tapered laminates, loaded via gripping their thick and thin ends, and a severely tapered laminate, loaded by contact at its tapered section, were investigated via experiments and high-fidelity finite element modelling. The primary failure mode is by delamination, initiated from a terminated ply in the tapered region, which is quite sensitive to a small delamination defect at a ply drop location. Experimental measurements and FE predictions correlate very well in all cases for both location and load. In the severely tapered case, the contact stress influences the delamination and so a fibre failure criterion also needs to be considered, including both the fibre direction tensile stress and its interaction with through-thickness direct and shear stresses imposed by the contact.

***Keywords**:* A. Laminates; B. Delamination; C. Cohesive interface modelling; Ply drops

* Corresponding author: *Email address*: b.zhang@bristol.ac.uk (Bing Zhang)

*DECLARATIONS OF INTEREST: NONE*

## 1. Introduction

Fibre-reinforced plastics (FRP) composites are increasingly being used in a wide range of industries, driven by their high strength-to-weight ratio, good corrosion resistance and excellent fatigue properties. To meet structural design requirements, e.g. aerodynamic and weight efficiency, it is often necessary to taper a composite component along one or multiple directions. This can be observed, for example, in a composite wind turbine blade, whose shell is tapered in the spanwise direction. The most common approach used to taper a composite laminate is dropping-off (terminating) internal or external plies at pre-defined locations [1]. At an internal ply drop as shown in Fig. 1. Two continuous sub-laminates ('base' and 'belt') enclose a dropped sub-laminate in the thick section, while either or both are curved, with the intention of re-connecting at the thin section. This creates a triangular resin pocket in the tapered region. Fig. 1 illustrates a symmetric ply drop, since the taper angles associated with the two continuous sub-laminates are the same [2]. By contrast, an asymmetric ply drop features different taper angles between the two belt plies, with the extreme case having the base sub-laminate as flat, with a corresponding taper angle of zero [3].

Due to these material and geometrical discontinuities, a tapered laminate is prone to interlaminar disbond (delamination) between these sub-laminates in the ply drop location, following earlier failure associated with the resin pocket [4,5]. A considerable amount of work has been reported in the literature on the failure mechanisms of tapered laminates under tensile loading [2–9]. As illustrated in Fig. 1, when a single ply drop undergoes pure tensile loading, the top and bottom interfaces between the discontinuous sub-laminate and the continuous sub-laminates experience interlaminar shear stress and through-thickness compression (TTC), which both show peak values at the end of the dropped plies and decrease towards the thick section [2,8,10]. In the thin section, these two continuous sub-laminates tend to separate due to the straightening out of their initially curved shape, thus leading to through-thickness tension at the interface between them. The interlaminar tensile stress shows a maximum at the toe of the resin pocket and decreases towards the thin section. Local bending of continuous sub-laminates occurs in the tapered region due to the curvature features. The specific stress characteristics near a ply drop are affected by several parameters, including the stacking sequence of the plies adjacent to the sensitive interfaces, the thickness of dropped sub-laminate, the taper angle and spacing between ply drops [2,9]. Based on the understanding of stress distribution near ply drops, a number of stress based and energy-release-rate (ERR) based approaches have been proposed to predict delamination onset and growth [1,7,11,12]. Useful optimisation methods of designing a tapered laminates were also presented based on a generic algorithm or stacking sequence tables [13–15].

Aiming at advancing the state of the art, this study employed an extensive experimental programme and high-fidelity finite element models to investigate the failure mechanisms of tapered laminates under tensile loading. The experimental programme, presented in Section 2, was performed to characterise the tensile failure mechanisms of tapered laminates considering the effects of ply drop spacing (taper angle) and interlaminar defects (represented by a steel film insert). A severely tapered laminate has also been characterised, held by a contact fixture at its tapered section and pulled at its thin section. Similar set-ups were explored in [16–18], but this study aims to give more detailed studies on laminates failure mechanisms using a high-fidelity 3D finite element modelling strategy. The high-fidelity FE modelling strategy is presented in Section 3 to predict the mechanical behaviour of these tapered laminates. Such a detailed modelling package and verification regarding tapered laminates is still missing in the literature. In Section 4, experimental observations and numerical predictions of the tensile failure mechanisms of these tapered laminates are presented and compared; Effects of the modelling parameters, including mesh size and cohesive parameters (strength pair and through-thickness compression enhancement factors) are discussed in detail. In Section 5, a fibre failure criterion, considering both the direct tensile stress and its interaction with through-thickness direct and shear stresses, is proposed and illustrated through the severely tapered laminate model.

## 2. Experimental programme

### *2.1. Specimen configurations*

Three taper angles of laminates were investigated in this study, two modestly tapered (Figs. 2a and b) and one severely tapered (Fig. 2c). All were manufactured from Hexcel's IM7/8552 prepreg material. For ease of description, the ply drops in each half of the tapered laminates are numbered in ascending order from the thin section (see Figs. 2). The two modestly tapered laminates have the same configuration, except for different ply drop spacings (d = 1.5 mm or 2 mm). Their thick sections have the symmetric stacking sequence of $[-45/0/\underline{45}/\underline{0}/\underline{-45}/\underline{0}/45/0/\underline{45}/\underline{0}/\underline{0}/\underline{-45}/0/45/0/-45]_S$, where the underscores indicates dropped plies, which leads to a 2:1 thickness ratio between the thick and thin sections. The nominal taper angles are 8.1° and 11.3° for the d = 2 mm and 1.5 mm tapered laminates, respectively. The nominal ply thickness is 0.25 mm. The severely tapered laminate also features a symmetric stacking sequence (Fig. 2c). It consists of a carbon fibre (IM7/8552) core laminate and two E-glass/914 glass FRP (GFRP) surface layers. GFRP skins were employed to provide protection due to the high frictional contact between the specimen and the loading rig used to hold the specimen during tensile testing. The specimen thickness reduces from a nominal 40.25 mm in the thick section to a nominal 11.75 mm in the thin section.

It was expected that delamination would be the critical failure mode, and so to further investigate the effect of potential manufacturing delamination defects, a 5 μm thick and 4 mm wide stainless-steel strip was inserted at ply drop 2 in each half of the 8.1° tapered laminate during lay-up to represent an artificial delamination. A previous study [19] has shown that 5 μm steel shim material provides the best approximation to a delamination in the case where no natural pre-crack can be developed. In summary, four configurations of laminates were tested: the 8.1° pristine tapered laminate, the 8.1° tapered laminate with artificial defect, the 11.3° pristine tapered laminate, and the pristine severely tapered laminate.

### *2.2. Specimen manufacture*

To produce the modestly tapered specimens, three panels were made (two for the pristine specimens with the two different ply drop spacings and one for the defect specimens). Each panel was made in two halves, with each half made by careful hand layup of Hexcel IM7/8552 prepreg of varying lengths onto a flat tool plate, vacuum bagging and then autoclave curing following the manufacturer's recommendations (2 h at 180 °C at 7 bar pressure). Placement of the thin steel strip was added into the lay-up process for the defect panel. Prior to insertion of the steel strip it was cleaned with acetone and coated with the Frekote 770-NC mould release agent. This surface treatment ensures that the metal insert is not bonded with the surrounding epoxy during the curing process and thereby behaves as an 'ideal' delamination. During lay-up, a debulking procedure of vacuum bagging at room temperature was performed after every fourth ply. After cure, the flat surface of each half of the panel was grit blasted and degreased, then Scotch-Weld AF 163-2 film adhesive was used to bond the two halves together. This was realised using a vacuum bag arrangement in an oven at 125 °C for 1 hour. The laminate panels were then carefully cut into individual specimens (15 mm wide and 250 mm long) using a CNC machine. To avoid grip damage during mechanical tests, GFRP tabs were bonded on to each end of the specimen on both sides, using an epoxy adhesive, leading to a 150 mm long gauge section.

The severely tapered panel was manufactured following a different procedure. Each half of the panel was laid up onto one half of an aluminium matched tool, which accommodated the panel within it during cure. A debulking procedure by vacuum bagging under room temperature was performed after every fourth ply. Once lay-up was complete, the two halves of the tooling were then brought together with the whole plate formed inside. A 30-minute debulking procedure under 1 bar vacuum and 50 °C was undertaken in order to reduce the separation between two halves of the plate caused by the bulk factor associated with ply terminations. Then, prior to cure in an autoclave, the tooling and the panel were vacuum bagged. A top plate made of aluminium was used to align the two halves of the matched tooling using two steel ball bearing guides. In consideration of

the large thickness of the panel and the large thermal mass of the tooling, the cure cycle was optimised to comprise several stages: 1) heating up to 180 °C from room temperature at the rate of 5 °C/min, 2) holding for 10 minutes, 3) cooling down to 120 °C, 4) holding for 65 minutes, 5) heating back to 180 °C at 5 °C/min, 6) holding for 200 minutes, and 7) cooling down to room temperature. The modified cure cycle allowed approximately achieving the manufacturer's recommended cure condition for the panel, i.e. 2 hours at 180 °C, without risking an exothermic reaction. In addition, a 7 bar pressure was applied from the start to close the residual separation between the two halves of the plate and full vacuum was maintained during cure. Following the curing process, a Vespel strip was bonded to the tapered region of the panel on each side, using an AF163 adhesive film that was cured under 1 bar vacuum and 125 °C for 1 hour. The Vespel strip further protected the specimen against wear damage due to the high contact stress between the specimen and the loading fixture, since it provided a lower friction coefficient than the GFRP skins. A CNC machine was employed to section the panel into individual specimens (Fig. 2c). At the thin end of each severely tapered specimen two GFRP tabs were bonded onto both sides using an epoxy adhesive, leading to a 170 mm long gauge section, which comprises the full thick section, the tapered section and the un-clamped part of the thin section.

### *2.3. Experimental set-up*

Seven specimens were tested for each configuration of the modestly tapered laminates under 0.5 mm/min displacement control, using a calibrated Instron 8801 servo-hydraulic machine equipped with a 100 kN load cell (Fig. 3a). A Canon 550D HD camera was situated on one side of the specimen to record global deformation. On the other side of the specimen, a high-speed video camera Photron SA-1 was focused on the tapered section to capture local damage.

Five specimens were tested for the severely tapered configuration using the experimental set-up shown in Fig. 3b. Each specimen was loaded under 2.5 mm/min displacement control using a calibrated Dartec MJ6290 servo hydraulic machine equipped with a 500 KN load cell. The machine crosshead gripped the thin section of the specimen with a 140 mm clamping length, while a custom-designed metal fixture held the coupon at its tapered region (Fig. 3c). This allowed clamping the tapered section when it was pulled at its thin section. The main body of the tapered-section holder was made of steel, but it had two titanium contact pads inserted to directly contact with the specimen (Fig. 3c). Two strain gauges were attached to the top and bottom surfaces of the specimen, at around 100 mm distance from the thick end. The high-speed Photron SA-1 video camera was also used to capture the delamination location for the severely tapered specimens.

## 3. High-fidelity modelling

### *3.1. Full meshes*

The meshing tool presented in [20] was further improved to create high-fidelity meshes for all the tapered laminates considered in this study. Locations of all CFRP plies were determined by scanning the well-polished side of a pre-tested specimen. Each ply drop in these tapered laminates was assumed to be a symmetric ply drop (see Fig. 1), according to microscopic observations of ply drops in the specimen. Experimental observation also showed that there is a slight thinning of the dropped ply, just before it ends at the resin pocket. It was estimated from microscopic observations that the thinning length was 0.4 mm, and the resin pocket was 1.2 mm long. These two parameters in conjunction with a cosine function can be used to produce an accurate representation of terminating/continuous plies and the resin pocket at a ply drop location, as shown in Fig. 4a. The meshing tool also allowed inserting cohesive elements between two adjacent plies, and between a resin pocket and its two neighbouring plies. These cohesive elements followed an interlaminar failure criterion, which will be described in the next sub-section. The pre-inserted metal strip is directly described by thin hexahedral elements inserted along the metal strip path, in conjunction with a frictionless contact defined between the thin elements and neighbouring resin-pocket/ply elements, as shown in Fig. 4b. Fig. 5 illustrates that the mesh generation technique allows accurate representation of the whole tapered specimen, typically including post-cure ply thickness, slightly asymmetric distributions of ply drops relative to the laminate mid-plane, as well as ply waviness which is particularly true for the central 0 plies of the severely tapered laminate. Note that all the specimens associated with each of the four configurations (8.1° pristine, 8.1° defect, 11.3° pristine and the severely tapered one) were cut from a single panel, thus there was no notable difference amongst specimens of the same configuration regarding their geometry and locations of ply drops; this point was verified by microscopic observations. It means that the specimen to specimen variation of a given configuration was not significant and can be represented by one high-fidelity mesh.

All these baseline tapered models considered here share some common features: 1) each ply was meshed as a one-element thick layer; 2) the whole gauge section length and full width of the tapered laminates were included in the FE models; 3) the element size along the laminate length was 0.1 mm in the tapered section and gradually increased towards both ends of the model; and 4) the element size along the laminate width was 0.5 mm. The tapered-section holder in the severely tapered laminate model was simplified into two curved rigid bodies in the numerical model with the front curvature of the holder being accurately described in the model. Overall, the 8.1° modestly tapered model has 256,260 single integration point (IP) hexahedral elements for plies, 6,030 single-IP

hexahedral elements for resin pockets, 238,890 four-IP cohesive elements for interlaminar interfaces, 12,060 four-IP cohesive elements for ply/resin-pocket interfaces and 544,050 nodes. The 11.3° modestly tapered model has 237,690 four-IP hexahedral elements for plies, 6,000 single-IP hexahedral elements for resin pockets, 221,400 four-IP cohesive elements for interlaminar interfaces, 12,000 four-IP cohesive elements for ply/resin-pocket interfaces and 505,610 nodes. The metal insert is described by 2,340 single-IP hexahedral elements in the defect model. The severely tapered laminate model consisted of 2,269,760 single-IP hexahedral elements for plies, 50,480 single-IP hexahedral elements for resin pockets, 1,900,000 four-IP cohesive elements for interlaminar interfaces, 100,960 four-IP cohesive elements for ply/resin-pocket interfaces, 8,320 single-IP hexahedral elements for the tapered-section holder and 4,484,334 nodes.

### *3.2. Ply material properties*

The elastic properties used in the models for the CFRP plies and resin pockets are given in Table 1 [21–23], where the homogenised properties of GFRP tabs in the severely tapered case were derived by classical laminate theory using the ply properties given in [24] and assuming that the GFRP plies show the same coefficients of thermal expansion as the CFRP ply. One thing that needs to be highlighted is that local material axes were defined using the mid-planes of elements instead of nodes, which allows better representation of fibre orientations around ply drops. The in-plane and through-thickness non-linear shear behaviour of the CFRP plies was described by:

$$\tau_{1i} = A \cdot sgn(\gamma_{1i}) \cdot \left(1 - e^{-B|\gamma_{1i}|}\right) \qquad i = 2, 3 \tag{1}$$

where the controlling parameters A and B were respectively assigned 138 MPa and 45 by fitting experimental data [23,25], while unloading was linearly controlled by the initial stiffness. The parameter A has the same unit as stress, while the parameter B is unit-less since strain ($\gamma_{1i}$) is unit-less. The Young's modulus and Poisson' ratio used for the stainless-steel insert in the defect model were respectively 190 GPa and 0.265.

### *3.3. Interlaminar failure*

There was no matrix cracking and fibre breakage observed in any of the tapered specimens prior to delamination, thus only delamination was considered in the high-fidelity modelling. Interlaminar interfaces are described by a bi-linear traction-separation cohesive formulation, as developed in [26,27]. Pure mode tractions ($\sigma_{\mathrm{I}}$ and $\sigma_{\mathrm{II}}$) and separations ($\delta_{\mathrm{I}}$ and $\delta_{\mathrm{II}}$) prior to failure are linearly related by an elastic stiffness ($K_{\mathrm{I}}$ and $K_{\mathrm{II}}$); the symbols I and II indicate mode I (opening) and mode II (shearing), respectively. Failure is initiated when Eq. 2 is satisfied.

$$\left(\frac{\langle\sigma_{\mathrm{I}}\rangle}{S_{\mathrm{I}}}\right)^2 + \left(\frac{\sigma_{\mathrm{II}}}{S_{\mathrm{II,E}}}\right)^2 = 1 \tag{2}$$

where $S_{\mathrm{I}}$ is mode I strength; the Macaulay operator $\langle\cdot\rangle$ is defined as $\langle x\rangle = \frac{1}{2}(x + |x|)$; $S_{\mathrm{II,E}}$ is the through-thickness compression enhanced mode II strength, as defined by:

$$S_{\mathrm{II,E}} = S_{\mathrm{II}} - \eta_{\mathrm{f}} \cdot min(0, \sigma_{\mathrm{I}}) \tag{3}$$

where $S_{\mathrm{II}}$ is the un-enhanced mode II strength; $\eta_{\mathrm{f}}$ represents the TTC strength enhancement factor. The mode I and II tractions in the stiffness degradation (softening) region are defined by:

$$\sigma_{\mathrm{I}} = (1 - D) \cdot S_{\mathrm{I}}; \quad \sigma_{\mathrm{II}} = (1 - D) \cdot S_{\mathrm{II,E}} \tag{4}$$

where *D* is the damage variable defined by:

$$D = \frac{\delta_{\mathrm{m}} - \delta_{\mathrm{m}}^{0}}{\delta_{\mathrm{m}}^{\mathrm{f}} - \delta_{\mathrm{m}}^{0}} \tag{5}$$

whereby $\delta_{\mathrm{m}}$ is the total mixed-mode relative displacement, defined by Eq. 6, which indicates that the mixed-mode separation does not take compression into account; The damage variable increases from 0 at failure initiation to 1 at complete failure. $\delta_{\mathrm{m}}^{0}$ and $\delta_{\mathrm{m}}^{\mathrm{f}}$ are the values of $\delta_{\mathrm{m}}$ at failure initiation and complete failure, respectively.

$$\delta_{\mathrm{m}} = \sqrt{\max(0, \delta_{\mathrm{I}})^2 + {\delta_{\mathrm{II}}}^2} \tag{6}$$

Complete interface failure is controlled by:

$$\left(\frac{G_{\mathrm{I}}}{G_{\mathrm{IC}}}\right)^{\theta} + \left(\frac{G_{\mathrm{II}}}{G_{\mathrm{IIC,E}}}\right)^{\theta} = 1 \tag{7}$$

where $G_{\mathrm{I}}$ and $G_{\mathrm{II}}$ are mode I and mode II energy release rates; mode ratio is here defined as the ratio of $G_{\mathrm{II}}$ to the sum of $G_{\mathrm{I}}$ and $G_{\mathrm{II}}$. $G_{\mathrm{IC}}$ is mode I critical ERR, while $G_{\mathrm{IIC,E}}$ indicates the mode II critical ERR enhanced due to TTC. The power $\theta \in [1,2]$ is an empirical factor derived from mixed-mode tests for interlaminar interfaces. The $G_{\mathrm{IIC,E}}$ value is determined by:

$$G_{\mathrm{IIC,E}} = \left(\frac{S_{\mathrm{II,E}}}{S_{\mathrm{II}}}\right)^{2} G_{\mathrm{IIC}} \tag{8}$$

where $G_{\mathrm{IIC}}$ is mode II critical ERR without TTC. Material properties assigned to the cohesive elements are listed in Table 2 [21,28]. The cohesive stiffness pair ($K_{\mathrm{I}}$ and $K_{\mathrm{II}}$) was deducted from the tensile modulus and Poisson's ratio of 8552 resin system [29] by considering the ratio between the geometric thickness (0.01 mm) and constitutive thickness (unity) of the interface cohesive elements. The fracture toughness pair ($G_{\mathrm{IC}}$ and $G_{\mathrm{IIC}}$) follows Refs. [30,31]. There exists discrepancy in the literature regarding the cohesive strength pair [21,23,26,29,32–37] and the TTC enhancement factor [28,38,39]. The reason why [60 MPa, 90 MPa] is used here as the baseline cohesive strength pair is simply because that it has been proved to give satisfactory predictions for many of the previous IM7/8552 laminate models [21,23,26,31,40,41]. Effects of the strength pair

and the TTC enhancement factor on the numerical predictions in these tapered cases will be discussed in Section 4.3.

### *3.4. Other model details*

The tapered models were computed using the commercial explicit Finite Element package LS-DYNA® in two consecutive steps. In the first step, a temperature field with a -160 °C differential was imposed to the full model to simulate post-cure cool down, which is known to be a significant cause of residual stresses during the composites manufacturing process. The temperature field was kept constant in the second step, where tensile loading was introduced. Tensile loading was applied to the modestly tapered models via constraining the left-edge nodes and assigning displacement to the right-edge nodes. Regarding the severely tapered model, mechanical loading was applied via the combination of a displacement boundary condition applied to the right end of the model and a full constraint applied to the two halves of the tapered-section holder. Contact between the tapered-section holder and two GFRP skins was defined by the well-known penalty algorithm [42] with a friction coefficient of 0.1, by referring to the literature values for polymer to metal contact [43,44].

## 4. Experimental observations and model validation

### *4.1. Modestly tapered laminate*

#### *4.1.1. Experimental observations*

The two modestly tapered pristine laminates generally showed a linearly increasing load response prior to a significant load drop. The high-speed images, as shown in Fig. 6a, taken during the test of an 8.1° pristine tapered laminate show that failure initiated in the form of small delamination cracks in the top and bottom continuous-ply/dropped-ply interfaces of ply drop 1 in the bottom half of the laminate. Delamination rapidly propagated at the 0°/0° interfaces towards the thick end of the specimen. Once the delamination started to propagate towards the thick end, enough energy was also available to drive the crack towards the thin section of the specimen, resulting in significant damage and significant reduction in load-bearing capability. The averaged peak load due to delamination was 60.78 kN with a CV (coefficient of variation) of 3.3% for the 8.1° pristine laminate (specifically, 59.69 kN, 58.83 kN, 58.24 kN, 63.29 kN, 62.40 kN, 62.69 kN and 60.35 kN for individual specimens), while it was 57.10 kN with a CV of 7.7% in the 11.3° pristine case (specifically, 54.78 kN, 56.60 kN, 54.88 kN, 51.57 kN, 64.58 kN, 55.86 kN and 61.25 kN for individual specimens).

The behaviour of the tapered specimens with artificially inserted defect featured a more progressive response. Following an initial linear-elastic response, a large crack initiated at the defect location (i.e. ply drop 2), which was accompanied by a load drop. The onset of delamination does not occur symmetrically at both defect

locations but initially favored one side. The second delamination crack initiating from the ply drop 1 occurred almost instantaneously and both cracks grew in a progressive manner, mainly towards the thin section. With slightly further loading, delamination occurred from the defect ply drop and ply drop 1 in the other half of the laminate, accompanied by a second load drop. Multiple delamination cracks shortly occurred along the core of the laminate between the first and second delamination cracks, which migrated across plies and coalesced to form larger delamination cracks. A significant load drop was observed at this point. The averaged peak load corresponding to the first delamination caused load drop was 33.83 kN with a CV of 4.37% for the defect case (specifically, 32.90 kN, 32.85 kN, 32.30 kN, 32.67 kN, 33.73 kN, 35.03 kN and 30.30 kN for individual specimens).

#### *4.1.2. Model validation*

The high-fidelity modelling revealed residual stress due to post-cure cool down in each modestly tapered case, however, no interlaminar failure was induced in the thermal step. The reaction load predicted by the numerical model features a monotonic increase with loading, until an apparent load drop due to delamination. Quantitatively, good numerical prediction has been achieved regarding the peak load due to delamination in all the modestly tapered cases, as shown in Fig. 7. The slight numerical underestimation in the 8.1° pristine case may be attributed to the effect of fibre bridging on mode I fracture toughness, which would lead to a larger $G_{\mathrm{IC}}$ value than the one given in Table 2 [45]. The location where delamination initiated was correctly predicted by the high-fidelity modelling for each case, i.e. ply drop 1 in the pristine tapered laminates and ply drop 2 in the defect tapered laminate (refer to Figs. 2a-b). The relatively progressive failure response in the defect case was also generally predicted by the numerical modelling. In more details, in these two modestly tapered pristine models, cracking initiated from the interfaces between the resin pocket and the top and bottom continuous plies (refer to Fig. 1) of ply drop 1. With slightly further loading, the cracking simultaneously propagated across the top and bottom continuous-ply/dropped-ply interfaces, the top and bottom resin-pocket/ply interfaces, as well as the continuous plies interface of ply drop 1. The rapid crack propagation caused an apparent load drop, which corresponds to the peak load plotted in Fig. 7. The mode ratio, $G_{\mathrm{II}}/(G_{\mathrm{I}}+G_{\mathrm{II}})$, at these interfaces associated with ply drop 1 were also extracted from the FE models. The top and bottom continuous-ply/dropped-ply interfaces of ply drop 1 experienced a close to pure mode II loading with some through-thickness compression. The mode ratio of the top and bottom resin-pocket/ply interfaces shifted from mode II at the thick-section side to mode I at the thin-section side, while the continuous plies interface experienced mainly mode I loading. When delamination happened from ply drop 1, the tips of the continuous-ply/dropped-ply interfaces and the resin-

pocket/ply interfaces associated with the ply drops 3 and 4 had also entered the softening region of the cohesive law. In the defect tapered case, delamination initiated from the interface between the two continuous plies in front of the artificial insert, then propagated towards the thin section. This was a mode I failure case. When delamination initiated in the defect case, all the cohesive elements associated with other ply drops remained deforming elastically.

In short, the 11.3° tapered laminate, featuring a 1.5 mm ply-drop spacing exhibited a slightly lower peak load due to delamination than the 8.1° tapered laminate with a 2 mm ply-drop spacing. This suggests that the step spacing could have an effect on delamination-driven failure, particularly if the step spacing is small enough to encourage interaction between adjacent ply drops [2]. The tensile loading response of a tapered laminate is quite sensitive to a pre-crack existing at a ply drop, as confirmed in Fig. 7.

### *4.2. Severely tapered laminate*

#### *4.2.1 Experimental observations*

The tensile load of a severely tapered laminate showed a modest increase at the beginning, which was attributed to the gradual development of non-linear contact forces between the specimen and the tapered-section holder. Once the contacts were well established, the reaction load showed a linear increase with displacement, until an apparent load drop occurred. The through-thickness compressive stresses in the tapered section also increased with loading. The load drop was caused by a delamination crack, which always happened just ahead of the high compressive region in the bottom half of all the severely tapered specimens. After being normalised by the averaged value, the peak loads corresponding to the delamination induced load drop were respectively 0.93, 0.93, 1.02, 1.05 and 1.06 for all the tested specimens. The delamination is expected to occur on one side of the specimen rather than exactly symmetric, due to the slightly asymmetric characteristics of ply drop locations and slightly wavy central 0° plies (see Fig. 5b). It was concluded from the high-speed camera data that delamination initiated amongst three adjacent ply drops, i.e. 1, 2 and 5, as indicated in Fig. 8a. It was however very difficult to tell exactly which one of these ply drops first invoked the delamination from the camera observation, even though a 360,000 frames/second frame rate was employed. The delamination rapidly propagated to the thin section clamped end, while it was suppressed in the tapered section due to the high through-thickness compression. The tests were terminated after observing the long interlaminar crack.

#### *4.2.2 Model validation*

The high-fidelity severely tapered model indicates that interlaminar failure was not induced due to post-cure cool down, but residual stresses existed throughout the whole model. The reaction load predicted by the

numerical model also features an initial build-up stage of the stable contact between the laminate and the tapered-section holder, and a monotonic increase with further loading until delamination. However, delamination location was not correctly predicted by the FE model using the baseline cohesive properties as listed in Table 2, and the peak load due to delamination was significantly underestimated by the FE model, as shown in Fig. 9. Note that all the load curves plotted here for the severely tapered laminates are normalised by the averaged peak load measured by experiments. The first delamination predicted by the FE model took place at the normalised load of 0.6 from the sixth interlaminar interface (counted from the CFRP core/GFRP skin interface) in front of the TTC region, as indicated by an arrow in Fig. 10a. As shown by the inset image in Fig. 10a, the mode ratio where the initial delamination happened was between 0.056 and 0.385, a mode I dominated failure case. This initial delamination was only at the edge of the laminate, and it did not propagate significantly. With slightly further loading, catastrophic delamination cracks happened at approximately the normalised load of 0.7 around the ply drops 1, 2 and 3 (see Fig. 10b), which was much lower than experimental average. This was due to a large ambient through-thickness tensile stress field prevailing in this region, as shown in Fig. 10c captured at 98.5% of the predicted delamination load. This makes the severely tapered laminate model a strength-dominated failure case, and so strongly influenced by the choice of the relatively low cohesive strength pair used [46], instead of a fracture-toughness-dominated damage propagation case, as is the situation for the modestly tapered specimens. For a strength-dominated failure initiation case, the cohesive strength pair used in the numerical modelling needs to be close to the real material mode I&II strengths of an interlaminar interface. For a fracture-toughness-dominated propagation case, the numerical mode I&II strength pair has been proved to show relatively less dependence on the material strengths, but it needs to be selected such that there are at least two to three cohesive elements in the cohesive zone [47–50]. Therefore, the cohesive mode I&II strength pair assigned to the severely tapered laminate model needs to be close to the real material mode I&II strength pair. There exists discrepancy on the material mode I&II strength pair of an IM7/8552 laminate interlaminar interface in the literature, with the mode I strength ranging from 60 MPa to 111 MPa and the mode II strength ranging from 82.6 MPa to 137 MPa [21,23,26,29,32–37,51]. A pair of close to middle values in the ranges, i.e. [90 MPa, 110 MPa] was selected as the cohesive mode I&II strength pair for the severely tapered laminate model. As shown in Fig. 9, the [90 MPa, 110 MPa] strength pair in combination with other cohesive properties listed in Table 2 gives good correlation with experimental measurement for the delamination load. The delamination location was also correctly predicted by the model using the new strength pair (Fig. 8b). The FE model slightly over-predicted the longitudinal strain values at delamination, extracted 100 mm from the thick end

(corresponding to the two strain gauge locations in experimental set-up), which may be attributed to the homogenisation of the GFRP tabs in the model.

As shown in Fig. 8b, the numerical model predicts that the first delamination happened at the ply drop 2 associated with the bottom half of the tapered laminate; the predicted delamination location agrees well with the experimental observation (comparing Fig. 8b to Fig. 8a). Regarding the failure mechanisms around the ply drop, initial cracking happened from its top resin-pocket/ply interface, then immediately the crack simultaneously propagated towards the thick section and the thin section of the laminate, respectively along the top continuous-ply/dropped-ply interface and the continuous plies interface. This was accompanied by an apparent load drop. There was much less damage in the bottom continuous-ply/dropped-ply interface and the bottom resin-pocket/ply interface before the load drop. The crack propagation towards the thick section was suppressed between the two tapered-section holders due to very high TTC enhancement. Fig. 11 provides the FE predicted through-thickness stress field at 99.0% of the predicted delamination load; the maximum compressive stress appears just underneath the curved ends of the tapered-section holder. The top continuous-ply/dropped-ply interface of the crack initiation ply drop was predominantly mode II loaded with slight TTC, while the bottom one featured a short distance of mode II region at the dropped-ply tip, followed by a large mixed-mode region. The top and bottom resin-pocket/ply interface and the continuous plies interface mainly experienced mode II dominated loading which was quite different from the modestly tapered laminate. Prior to delamination initiation, only the cohesive elements around the two forward ply drop pairs have entered the softening region of the traction-displacement law. All the interfaces between the two tapered-section holders remain in the elastic region, under pure mode II with high TTC.

### *4.3. Effects of modelling parameters*

*Mesh size*

All the tapered models were first run by varying the element length in the tapered region, which is more susceptible to damage than the thin & thick sections. The element width was kept at 0.5 mm. The [60 MPa, 90 MPa] strength pair was used for the modestly tapered models, while [90 MPa, 110 MPa] was used for the severely tapered model due to the reasons explained above. As shown in Fig. 12, the element size demonstrates negligible effect on the predictions of global loading stiffness and delamination location in all the cases. The two modestly tapered pristine models start to converge from 0.3 mm, while the severely tapered model starts to converge from 0.4 mm. The defect tapered model starts to converge from 0.1 mm. Similar to a DCB model, the defect tapered model also features a pre-crack (Fig. 4b) and the damage sensitive interface (i.e. the continuous

plies interface of ply drop 1 in front of the pre-insert) is mode I loaded, thus its mesh convergence trend is consistent with the mode I numerical cohesive zone length as derived by a DCB model and the requirement of at least two to three elements existing in the cohesive zone [21,23,26,29,32–37]. A DCB model with a very fine mesh (0.025 mm) was run following the procedures detailed in Refs. [49,50], and it gave the mode I numerical cohesive length at 0.6 mm for the strength pair of [60 MPa, 90 MPa] and 0.275 mm for the strength pair of [90 MPa, 110 MPa]. Differently, there were not pre-cracks assumed around the ply drops in the three pristine tapered models, and the interface elements around the damage sensitive ply drops featured a range of mode ratios. Thus, it was not straightforward to derive the convergence element length by a DCB, 4ENF or MMB test [50]. All the tapered models were also re-run with two other element widths (0.25 mm and 1 mm), apart from the baseline element width (0.5 mm). It was found that the element width showed negligible effect on the numerical predictions for all the tapered laminate models considered here.

*Cohesive strength pair*

As explained above, the numerical mode I&II strengths used for the severely tapered laminate modelling need to be close to the real material mode I&II strengths. These three modestly tapered laminate models were re-run using the cohesive strength pair assigned to the severely tapered laminate model, i.e. [90 MPa, 110 MPa]. The element size used for the strength pair parametric study was 0.1 mm. As shown in Fig. 13, the cohesive strength pair shows negligible effects on the global loading stiffness in all the modestly tapered cases. The defect tapered model shows no prediction difference when using the two strength pairs. This is because that the defect tapered model is a mode I dominated case, and at least two to three interface elements exist in the cohesive zone for both of the strength pairs. For the two pristine tapered laminate models, the [90 MPa, 110 MPa] strength pair predicted a slightly higher peak load due to delamination than the [60 MPa, 90 MPa] strength pair, but both correlate well with experimental measurements. These two cohesive pairs give a sufficiently accurate prediction of delamination location in all the modestly tapered cases.

*TTC enhancement definition*

There exists some variation in the literature regarding the definition of through-thickness compression enhancement [28,38,39]. In the current model the toughness enhancement is assumed to be equal to the square of the strength enhancement (Eq. 8). An alternative model, defined in Eq. 9, is to assume the toughness enhancement as an independent definition to the strength enhancement [28,31]:

$$G_{\mathrm{IIC,E}} = G_{\mathrm{IIC}}(1 - \eta_{\mathrm{G}} \cdot min(0, \sigma_{\mathrm{I}})) \tag{9}$$

where $\eta_{\mathrm{G}}$ is the TTC enhancement factor for mode II toughness. The severely tapered model and the two

modestly tapered models without defect were re-run by using the combination of Eq. 3 and Eq. 8 respectively for strength enhancement and mode II toughness enhancement (i.e. Law C in Ref. [28]) and the combination of Eq. 3 and Eq. 9 respectively for strength enhancement and mode II toughness enhancement (i.e. Law A in Ref. [28]). The modestly tapered model with defect is not suitable for this piece of study since its delamination is pure mode I opening dominated. Two other strength enhancement factors were tested (0.3 and 0.74) for Law C, apart from the baseline value 0.5. For Law A, the values suggested by Ref. [31], i.e. 0.3 and 0.064 for $\eta_{\mathrm{f}}$ and $\eta_{\mathrm{G}}$ were tested for these three tapered cases.

As shown in Fig. 14, these different TTC enhancement definitions show no effect on the global stiffness in all these tapered cases. Regarding the modestly tapered models, the predicted delamination locations show no difference amongst these TTC enhancement definitions. The delamination loads given by the three law C enhancement factors all show good agreement with experimental measurement. The law A enhancement definition shows a slight overestimate in the 8.1° modestly tapered case.

Regarding the severely tapered laminate, the FE results showed no apparent difference regarding both the load and location of delamination when the Law C enhancement factor was equal to or larger than 0.5 and for the Law A with the enhancement pair of [0.3, 0.064]. When the Law C enhancement factor was equal to 0.3 or 0.4, the FE model gave an incorrect delamination location and underestimated the delamination load. It can thus be summarised that the Law C TTC enhancement definition with an enhancement factor larger than 0.5 give satisfactory prediction regarding both delamination location and load for all these tapered cases. The reason why the Law A with the enhancement pair of [0.3, 0.064] is robust for the severely tapered case, but seems slightly conservative for the 8.1° modestly tapered case could be attributed to the fact that the enhancement pair of [0.3, 0.064] was derived by a linear regression on a series of TTC tests whereby a much higher through-thickness compressive stress was present than the modestly tapered laminate case studied here.

**5. Fibre failure**

Fibre failure was not observed prior to delamination in the specimens studied here, however, in the severely tapered laminate case the high through-thickness compression due to the tapered-section holders and relatively modest transverse compression due to the constraint by angled plies are expected to significantly degrade the longitudinal fibre tensile strength of the specimen [52–56], which is dominated by its 0° plies. FE modelling shows that large in-plane and through-thickness shear stresses were also present in the tapered section, which may further degrade the longitudinal tensile strength of the specimen. Gan et al. [56] derived a fibre failure criterion via experimental tests that combines the fibre-direction tensile and through-thickness compressive

stresses. Here, this fibre failure criterion is extended to the more general case of all possible interactions of fibre tensile stress with other stress components, including through-thickness and in-plane shear stresses as well as in-plane transverse compressive stresses. The new fibre failure criterion is thus expressed in a general form by:

$$d_{\mathrm{f}} = \frac{\langle \sigma_{11} \rangle - \alpha \cdot \min(0, \sigma_{33}) + \beta \cdot |\tau_{13}| - \gamma \cdot \min(0, \sigma_{22}) + \delta \cdot |\tau_{12}|}{S_{11\mathrm{U}}} \tag{10}$$

where fibre failure occurs when the damage variable $d_{\mathrm{f}}$ equals unity; $\alpha$, $\beta$, $\gamma$ and $\delta$ are the coefficients for individual stress components, which are defined in the local coordinate system of a lamina with its *1-direction* following its fibre direction. $S_{11\mathrm{U}}$ is the fibre-direction tensile strength of a unidirectional laminate. For the IM7/8552 laminates studied here, $S_{11\mathrm{U}}$ is equal to 2723 MPa, from the manufacturer's product datasheet [57].

To investigate the potential importance of including multiple stress components in the fibre failure criterion, the severely tapered model was re-run with the fibre failure criterion enabled. Specifically, five cases of the fibre failure criterion were tested;1) α=β=γ=δ=0, 2) α=1 and β=γ=δ=0, 3) α=β=1 and γ=δ=0, 4) α=β=γ=1 and δ=0, and 5) α=β=γ=δ=1. This allows evaluating the fibre health condition with the increasing number of stress components activated in the fibre failure criterion. At the point of delamination, all five cases of fibre failure criteria were not predicting any fibre breakage, which correlated well with experimental observations. The fibre damage variable fields in the 0° plies predicted by these five cases at the point of delamination are given in Fig. 15. It can be seen that the fibre failure variable shows its maximum in the thin section of the tapered laminate (around ply drop 1) when only the fibre-direction normal stress was considered in the fibre failure criterion, while the maximum of the fibre failure variable immediately moved to the thick tapered section for the other four stress combinations, as indicated by arrows in Fig. 15. Delamination happened before fibre failure in the severely tapered specimen studied here. If, however a more highly toughened matrix system was to be used, delamination could be suppressed. This means that fibre failure, which is a more critical failure mode, may occur before delamination. To study this scenario, the model was re-run with delamination artificially suppressed, by increasing the interfacial pure mode strengths and fracture toughness by a factor of 5. In this case, the FE results showed no delamination before fibre failure. Fibre failure initiated around the ply drop 1 in the thin section when only $\sigma_{11}$ was taken in account in the fibre failure criterion. More catastrophically, fibre failure happened in the thick tapered section for the other four stress combinations. The fibre failure load decreased with the number of stress components considered in the failure criterion. These show that the failure mode can change depending on properties. There is not enough experimental data currently available in the literature to fully validate the fibre failure models, but this work shows the importance of a correct fibre failure criterion capturing both the stress and damage interactions.

## 6. Concluding remarks

This paper has investigated the failure mechanisms of two modestly tapered laminates and a more severely tapered laminate, when subjected to tensile loading. The modestly tapered laminates were loaded via clamping at their thick and thin ends. The severely tapered laminate was pulled at its thin section, while its tapered section was held by a metal contact fixture. This study was carried out through a careful and detailed experimental programme and a high-fidelity modelling package. A thin stainless-steel thin strip was inserted at a selected ply drop location in one of the modestly tapered specimen configurations during manufacture, to study the effect of a delamination type defect on the mechanical response of a tapered laminate. High-fidelity models were created by an image-based mesh generation tool that allowed accurate representation of a tapered laminate, including post-cure ply thickness, ply drops and observed ply waviness. Interlaminar interfaces and the interfaces between resin pockets and neighbouring plies were all described by cohesive elements, which follow a bi-linear traction-separation law. Interlaminar shear enhancement due to the through-thickness compression was also incorporated into the cohesive law. The high-fidelity models gave good agreement with experimental measurements in the tapered cases, regarding both delamination load and location.

It was also found that when there exists a large ambient through-thickness tensile or shear stress field, as seen in the severely tapered laminate, the numerical mode I&II strength pair of cohesive elements needs to be close to the real material mode I&II strengths of interlaminar interfaces. Both modelling and experiments show that the tapered laminate with an 11.3° taper angle shows a lower peak load due to delamination than the tapered laminate with an 8.1° taper angle. The presence of a defect at a ply drop was found to severely reduce the mechanical performance of a tapered laminate. Shear enhancement due to through-thickness compression explains the observed phenomenon in the severely tapered laminate that delamination initiated from the thin section instead of the thick tapered section, where high interlaminar stresses existed. Parametric studies were also undertaken regarding the effects of element size, cohesive strength pair and TTC enhancement definitions on the numerical predictions in all cases.

A new fibre failure criterion has been proposed to take account of the full range of potential interactions with the 3D stress state that occurs in this case. It has been demonstrated that for the contact loaded severely tapered laminate, whose 0° plies exhibited high values of the different stress components in the tapered section, different levels of fibre damage were predicted, depending on which stress interactions were included. It has been demonstrated by the high-fidelity modelling that by artificially supressing delamination, fibre failure occurred in

the thin section if only the fibre-direction tensile stress was considered, while fibre failure may happen in the tapered section if other stress components were also considered in the criterion.

**CRediT authorship contribution statement**

**Bing Zhang:** Conceptualization, Methodology, Software, Validation, Formal analysis, Investigation, Writing - Original Draft. **Luiz F. Kawashita:** Conceptualization, Methodology, Software, Writing - Review & Editing. **Mike I. Jones:** Validation, Investigation, Resources. **James K. Lander:** Validation, Investigation, Resources. **Stephen R. Hallett:** Conceptualization, Methodology, Validation, Supervision, Writing - Review & Editing, Project administration, Funding acquisition.

**Acknowledgements**

The authors would like to acknowledge Rolls-Royce plc for the support of this research through the Composites University Technology Centre (UTC) at the University of Bristol, UK. Also, thanks to Alexander Kampe for the delamination defect experimental results, produced while on a student placement from TU Dresden.

**References**

[1] He K, Hoa SV, Ganesan R. The study of tapered laminated composite structures: a review. Compos Sci Technol 2000;60:2643–57.
[2] Cui W, Wisnom MR, Jones M. Effect of step spacing on delamination of tapered laminates. Compos Sci Technol 1994;52:39–46.
[3] Wisnom MR, Dixon R, Hill G. Delamination in asymmetrically tapered composites loaded in tension. Compos Struct 1996;35:309–22.
[4] Helmy S, Hoa S V. Tensile fatigue behavior of tapered glass fiber reinforced epoxy composites containing nanoclay. Compos Sci Technol 2014;102:10–9.
[5] Gan KW, Allegri G, Hallett SR. A simplified layered beam approach for predicting ply drop delamination in thick composite laminates. Mater Des 2016;108:570–80.
[6] Wisnom MR, Jones MI, Cui W. Failure of tapered composites under static and fatigue tension loading. AIAA J 1995;33:911–8.
[7] Allegri G, Wisnom MR, Hallett SR. A simplified approach to the damage tolerance design of asymmetric tapered laminates. Part I: Methodology development. Compos Part A Appl Sci Manuf 2010;41:1388–94.
[8] Vidyashankar BR, Krishna Murty A V. Analysis of laminates with ply drops. Compos Sci Technol 2001;61:749–58.
[9] Meirinhos G, Rocker J, Cabanac JP, Barrau JJ. Tapered laminates under static and fatigue tension loading. Compos Sci Technol 2002;62:597–603.
[10] Mukherjee A, Varughese B. Design guidelines for ply drop-off in laminated composite structures. Compos Part B Eng 2001;32:153–64.
[11] Cui WC, Wisnom MR, Jones M. A comparison of failure criteria to predict delamination of unidirectional glass/epoxy specimens waisted through the thickness. Composites 1992;23:158–66.
[12] Giannis S. Utilising fracture mechanics principles for predicting the mixed-mode delamination onset and growth in tapered composite laminates. Compos Struct 2013;102:294–305.
[13] Irisarri FX, Lasseigne A, Leroy FH, Le Riche R. Optimal design of laminated composite structures with ply drops using stacking sequence tables. Compos Struct 2014;107:559–69.
[14] Shrivastava S, Mohite PM, Limaye MD. Optimal design of fighter aircraft wing panels laminates under multi-load case environment by ply-drop and ply-migrations. Compos Struct 2019;207:909–22.
[15] York CB. On tapered warp-free laminates with single-ply terminations. Compos Part A Appl Sci Manuf 2015;72:127–38.

[16] Kogo Y, Hatta H, Toyoda M, Sugibayashi T. Application of three-dimensionally reinforced carbon-carbon composites to dovetail joint structures. Compos Sci Technol 2002;62:2143–52.
[17] Hatta H, Goto K, Sato T, Tanatsugu N. Applications of carbon-carbon composites to an engine for a future space vehicle. Adv Compos Mater 2003;12:237–59.
[18] Semb G, Gradin PA, Hallgren I. An analytical study of a composite dovetail joint. J Compos Mater 2003;37:99–109.
[19] Le Cahain YM, Noden J, Hallett SR. Effect of insert material on artificial delamination performance in composite laminates. J Compos Mater 2015;49:2589–97.
[20] Kawashita L, Jones MI, Hallett SR, Wisnom MR, Giannis S. High fidelity modelling of tapered laminates with internal ply terminations. 18th Int. Conf. Compos. Mater., Jeju Island, Korean: 2011, p. 1–6.
[21] Hallett SR, Green BG, Jiang WG, Wisnom MR. An experimental and numerical investigation into the damage mechanisms in notched composites. Compos Part A Appl Sci Manuf 2009;40:613–24.
[22] Zhang B, Allegri G, Yasaee M, Hallett SR, Partridge IK. On the strain and delamination sensing functions of CFRP Z-pins. Compos Sci Technol 2015;Under revi:1–25.
[23] Mukhopadhyay S, Jones MI, Hallett SR. Compressive failure of laminates containing an embedded wrinkle; Experimental and numerical study. Compos Part A Appl Sci Manuf 2015;73:132–42.
[24] Gilchrist MD, Kinloch AJ, Matthews FL, Osiyemi SO. Mechanical performance of carbon-fibre-and glass-fibre-reinforced epoxy I-beams: I. Mechanical behaviour. Compos Sci Technol 1996;56:37–53.
[25] Makeev A, Seon G, Lee E. Failure predictions for carbon/epoxy tape laminates with wavy plies. J Compos Mater 2010;44:95–112.
[26] Jiang W-G, Hallett SR, Green BG, Wisnom MR. A concise interface constitutive law for analysis of delamination and splitting in composite materials and its application to scaled notched tensile specimens. Int J Numer Methods Eng 2007;69:1982–95.
[27] Li X, Hallett SR, Wisnom MR. A finite element based statistical model for progressive tensile fibre failure in composite laminates. Compos Part B Eng 2013;45:433–9.
[28] Li X, Hallett SR, Wisnom MR. Predicting the effect of through-thickness compressive stress on delamination using interface elements. Compos Part A Appl Sci Manuf 2008;39:218–30.
[29] HEXCEL. HexPly® 8552 epoxy matrix product data sheet. 2016.
[30] O'Brien TK, Johnston WM, Toland GJ. Mode II interlaminar fracture toughness and fatigue characterization of a graphite epoxy composite material. NASA Tech Rep NASA/TM-2010-216838 2010:1–32.
[31] Xu X, Wisnom MR, Sun X, Rev T, Hallett SR. Experimental determination of Through-Thickness Compression (TTC) enhancement factor for Mode II fracture energy. Compos Sci Technol 2018;165:66–73.
[32] Lemanski SL, Wang J, Sutcliffe MPF, Potter KD, Wisnom MR. Modelling failure of composite specimens with defects under compression loading. Compos Part A Appl Sci Manuf 2013;48:26–36.
[33] Charalambous G, Allegri G, Lander JK, Hallett SR. A cut-ply specimen for the mixed-mode fracture toughness and fatigue characterisation of FRPs. Compos Part A Appl Sci Manuf 2015;74:77–87.
[34] Nikishkov Y, Makeev A, Seon G. Progressive fatigue damage simulation method for composites. Int J Fatigue 2013;48:266–79.
[35] Camanho PP, Maimí P, Dávila CG. Prediction of size effects in notched laminates using continuum damage mechanics. Compos Sci Technol 2007;67:2715–27.
[36] Wanthal S, Schaefer J, Justusson B, Hyder I, Engelstad S, Rose C. Verification and Validation Process for Progressive Damage and Failure Analysis Methods in the NASA Advanced Composites Consortium. Am. Soc. Compos. Tech. Conf., Purdue University, West Lafayette: 2017.
[37] Lee J, Soutis C. Measuring the notched compressive strength of composite laminates: Specimen size effects. Compos Sci Technol 2008;68:2359–66.
[38] Gan KW, Hallett SR, Wisnom MR. Measurement and modelling of interlaminar shear strength enhancement under moderate through-thickness compression. Compos Part A Appl Sci Manuf 2013;49:18–25.
[39] Zou Z, Lee H. A cohesive zone model taking account of the effect of through-thickness compression. Compos Part A Appl Sci Manuf 2017;98:90–8.
[40] Mukhopadhyay S, Nixon-Pearson OJ, Hallett SR. An experimental and numerical study on fatigue damage development in laminates containing embedded wrinkle defects. Int J Fatigue 2018;107:1–12.
[41] Nixon-Pearson OJ, Hallett SR, Harper PW, Kawashita LF. Damage development in open-hole composite specimens in fatigue. Part 2: Numerical modelling. Compos Struct 2013;106:890–8.
[42] Hallquist JO, Goudreau GL, Benson DJ. Sliding interfaces with contact-impact in large-scale Lagrangian

computations. Comput Methods Appl Mech Eng 1985;51:107–37.
[43] Mens JWM, de Gee AWJ. Friction and wear behaviour of 18 polymers in contact with steel in environments of air and water. Wear 1991;149:255–68.
[44] Quaglini V, Dubini P. Friction of polymers sliding on smooth surfaces. Adv Tribol 2011;2011.
[45] Murri GB. Evaluation of delamination onset and growth characterization methods under mode I fatigue loading. NASA Tech Rep NASA/TM-2013-217966 2013:1–27.
[46] May M, Hallett SR. A combined model for initiation and propagation of damage under fatigue loading for cohesive interface elements. Compos Part A Appl Sci Manuf 2010;41:1787–96.
[47] Turon A, Dávila CG, Camanho PP, Costa J. An engineering solution for mesh size effects in the simulation of delamination using cohesive zone models. Eng Fract Mech 2007;74:1665–82.
[48] Turon A, Camanho PP, Costa J, Renart J. Accurate simulation of delamination growth under mixed-mode loading using cohesive elements: Definition of interlaminar strengths and elastic stiffness. Compos Struct 2010;92:1857–64.
[49] Harper PW, Hallett SR. Cohesive zone length in numerical simulations of composite delamination. Eng Fract Mech 2008;75:4774–92.
[50] Harper PW, Sun L, Hallett SR. A study on the influence of cohesive zone interface element strength parameters on mixed mode behaviour. Compos Part A Appl Sci Manuf 2012;43:722–34.
[51] Adluru HK, Hoos KH, Iarve E V., Ratcliffe JG. Delamination initiation and migration modeling in clamped tapered laminated beam specimens under static loading. Compos Part A Appl Sci Manuf 2019;118:202–12.
[52] Hine PJ, Duckett RA, Kaddour AS, Hinton MJ, Wells GM. The effect of hydrostatic pressure on the mechanical properties of glass fibre/epoxy unidirectional composites. Compos Part A Appl Sci Manuf 2005;36:279–89.
[53] Zinoviev PA, Tsvetkov S V. Mechanical properties of unidirectional organic-fibre-reinforced plastics under hydrostatic pressure. Compos Sci Technol 1998;58:31–9.
[54] Parry TV, Wronski AS. The effect of hydrostatic pressure on the tensile properties of pultruded CFRP. J Mater Sci 1985;20:2141–7.
[55] Zinoviev PA, Tsvetkov S V., Kulish GG, Van Den Berg RW, Van Schepdael LJMM. The behavior of high-strength unidirectional composites under tension with superposed hydrostatic pressure. Compos Sci Technol 2001;61:1151–61.
[56] Gan KW, Wisnom MR, Hallett SR. Effect of high through-thickness compressive stress on fibre direction tensile strength of carbon/epoxy composite laminates. Compos Sci Technol 2014;90:1–8.
[57] HEXCEL. HexTow® IM7 carbon fibre product data sheet. 2014.

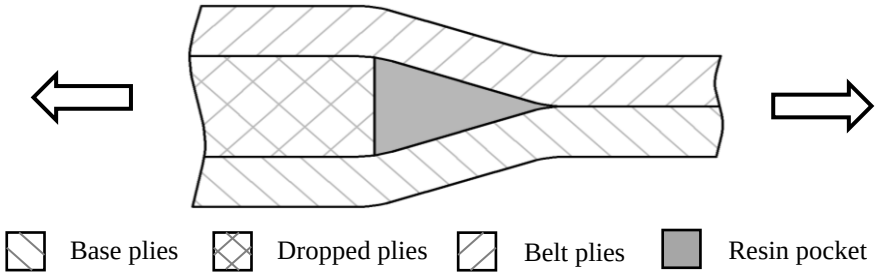


Fig. 1. Schematics of a symmetric ply drop.

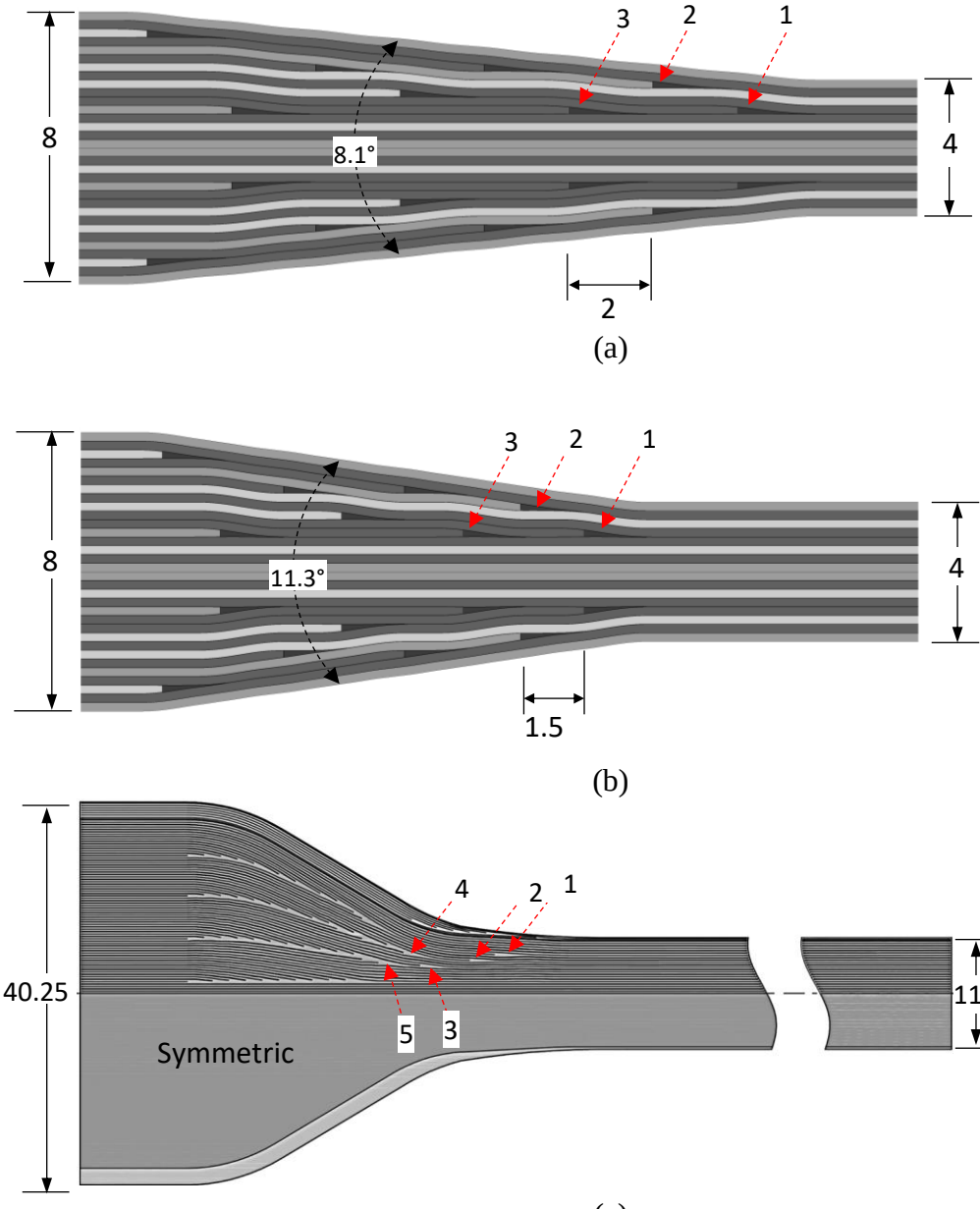


Fig. 2. Schematics of the (a) 8.1° tapered laminate, (b) the 11.3° tapered laminate and (c) the severely tapered laminate (unit: mm).

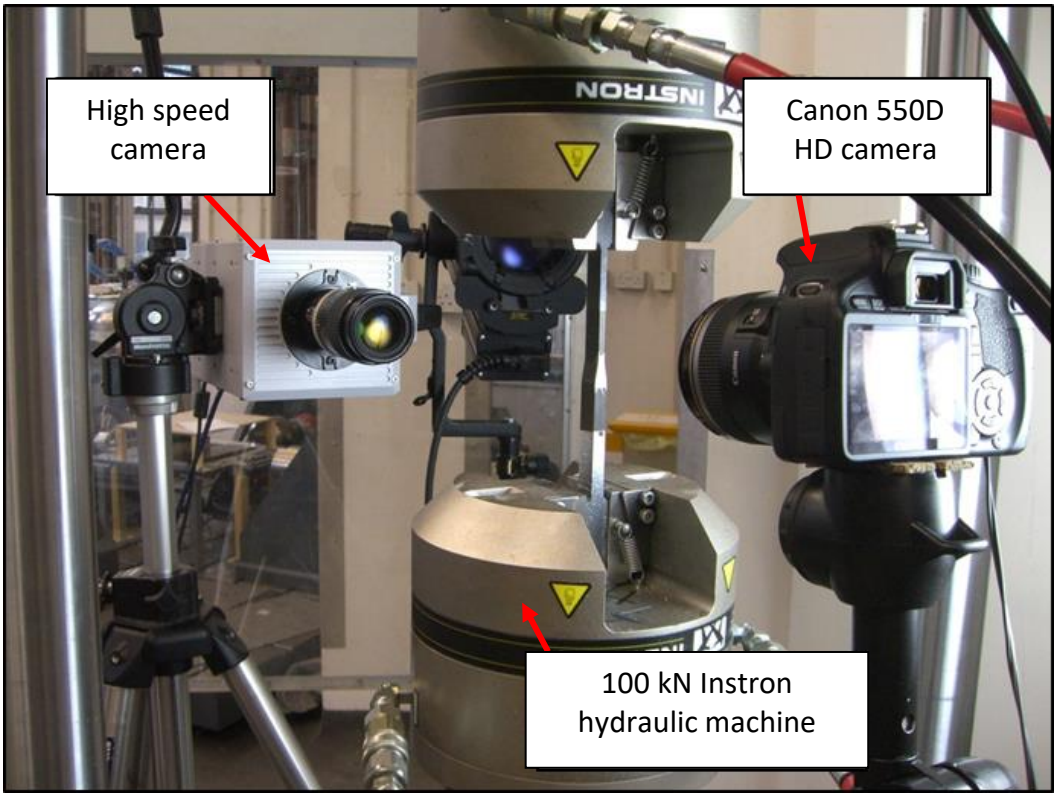


(a)

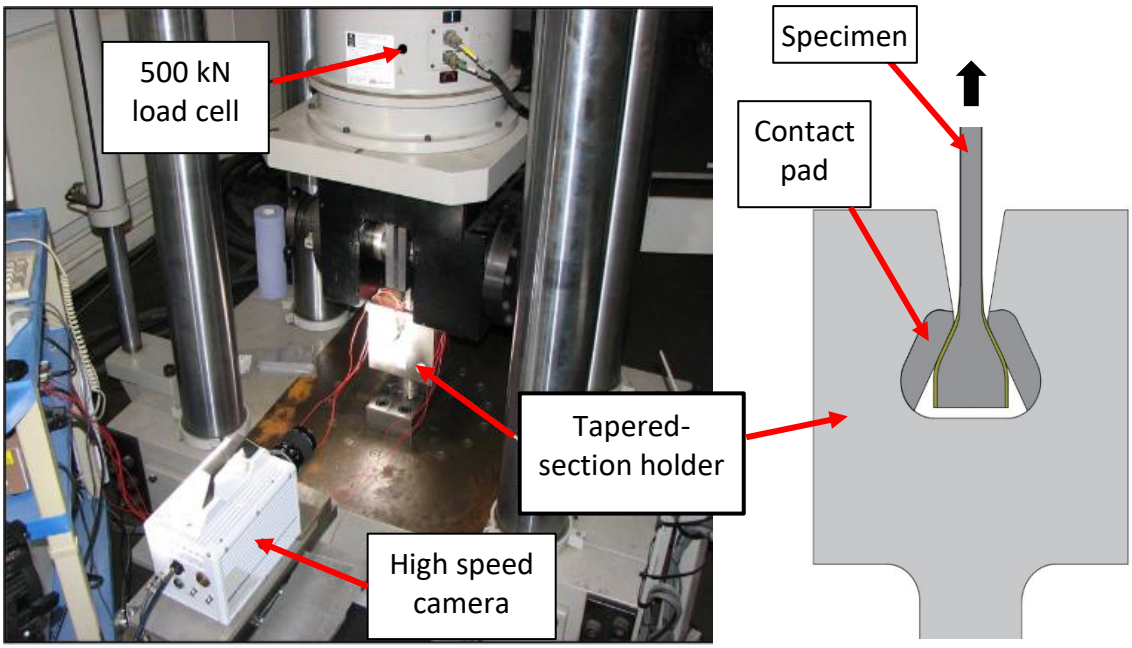


(b) (c)

Fig. 3. (a) Experimental set-up for the modestly tapered specimens; (b) experimental set-up for the severely tapered specimens; (c) schematic illustration of the tapered-section holder used to load the severely tapered specimens.

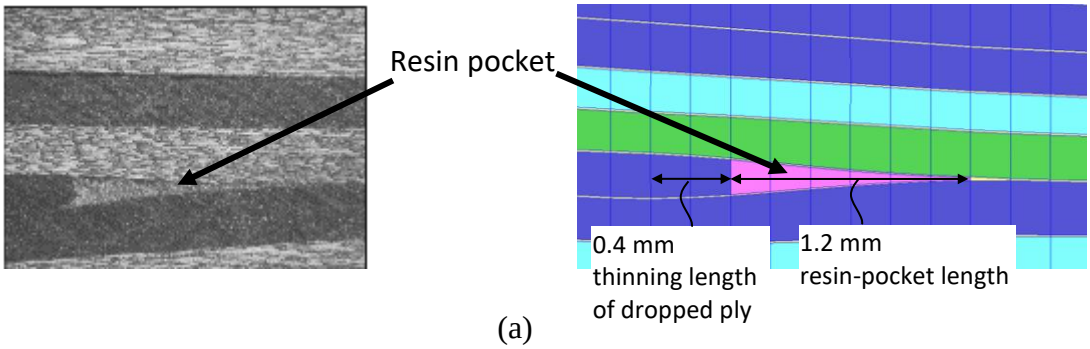


(a)

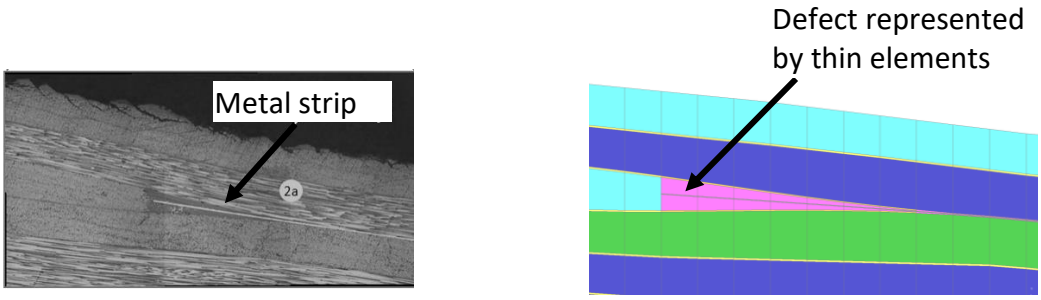


(b)

Fig. 4. Comparisons between (left) microscopic observations and (right) numerical descriptions of (a) a pristine ply drop and (b) a ply drop with an artificially inserted defect.

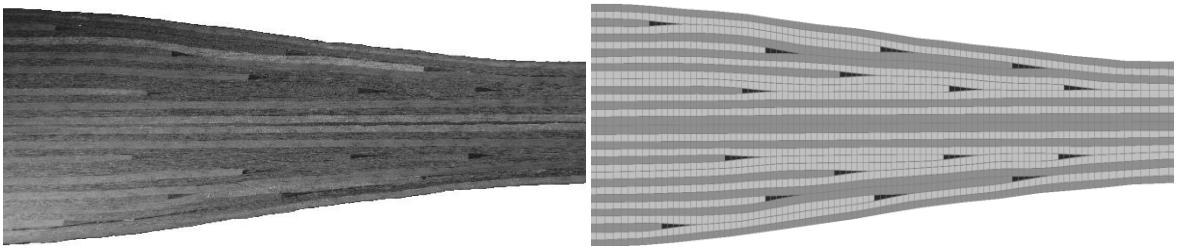

(a)

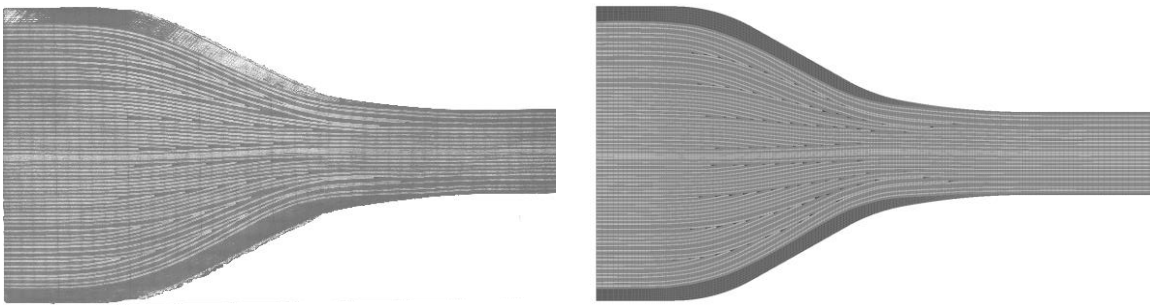

(b)

Fig. 5. Comparisons of (left) the microscopic observations and (right) numerical meshes for (a) the 8.1° modestly tapered laminate and (b) the severely tapered laminate.

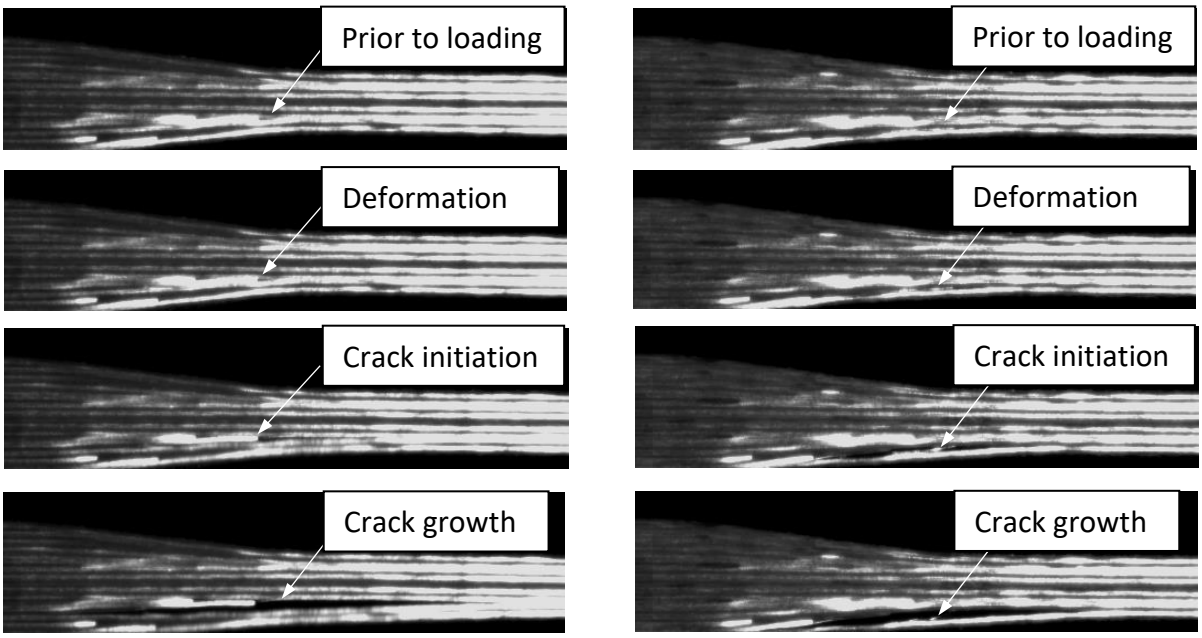


Fig. 6. High-speed images ordered in sequence showing the crack formation process of (a) an 8.1° pristine tapered specimen and (b) an 8.1° defect tapered specimen with artificial defect.

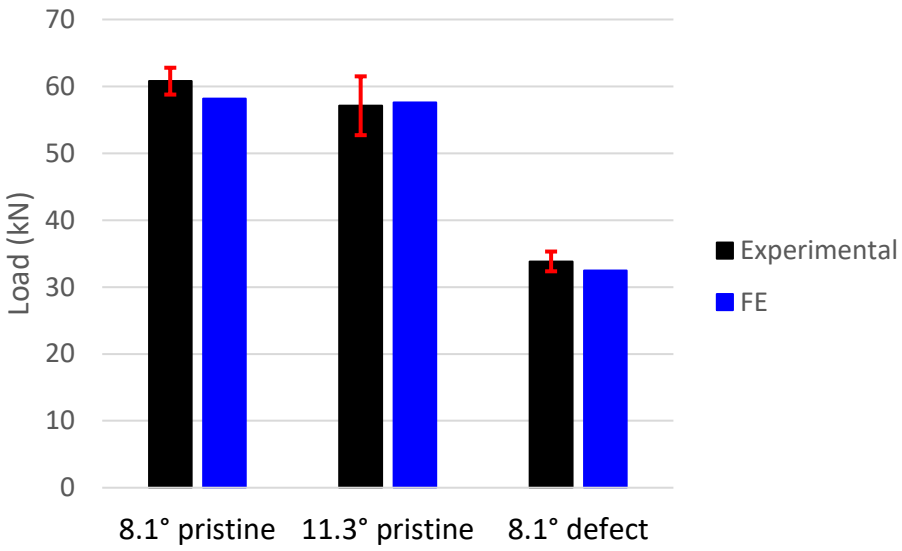


Fig. 7. Comparison between FE predicted and experimentallly measured peak loads due to delamination for the modestly tapered laminates.

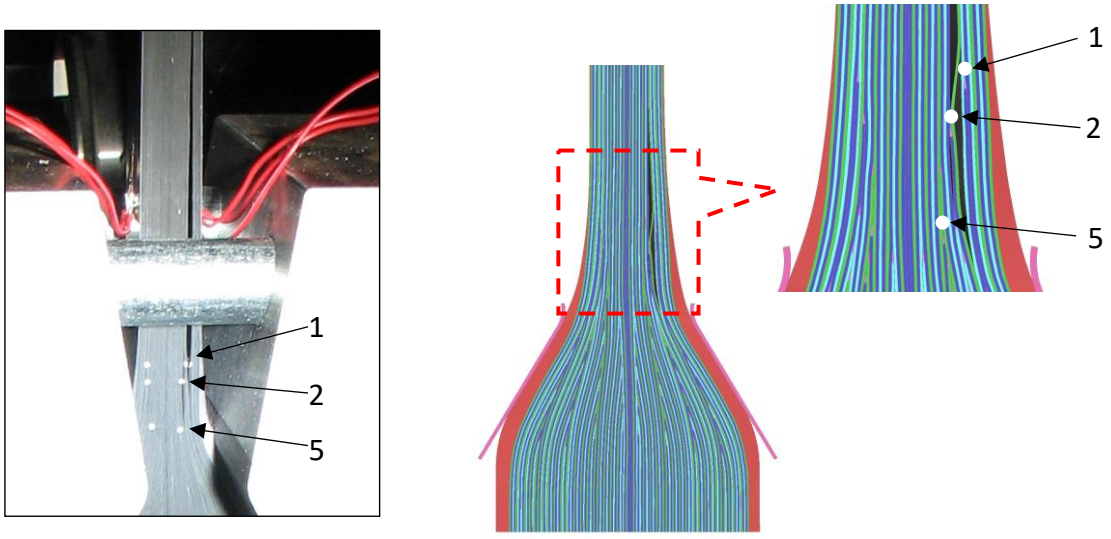


(a) (b)

Fig. 8. Comparison of (a) experimentally observed failure location and (b) FE predicted delamination location; white dots indicate the ply drops 1, 2 and 5.

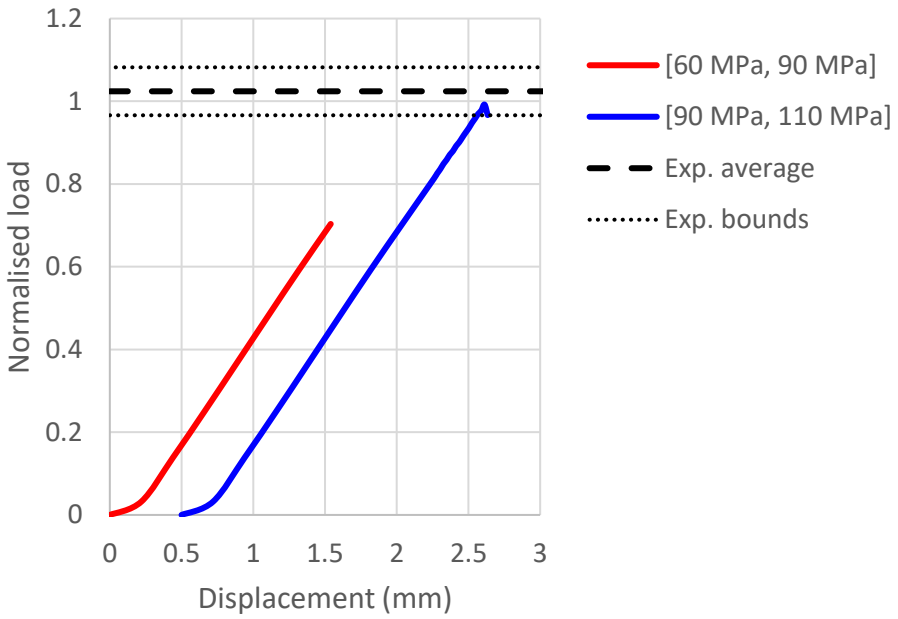


Fig. 9. Comparisons between experimental measurements and FE predictions using two cohesive strength pairs.

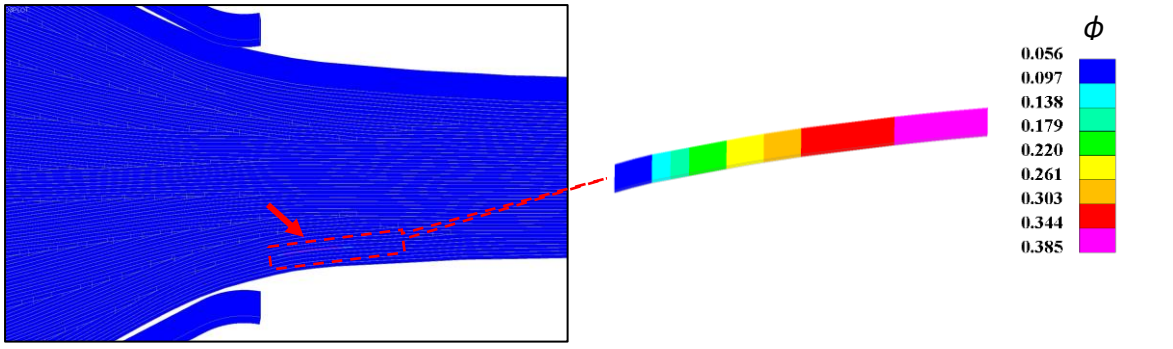


(a)

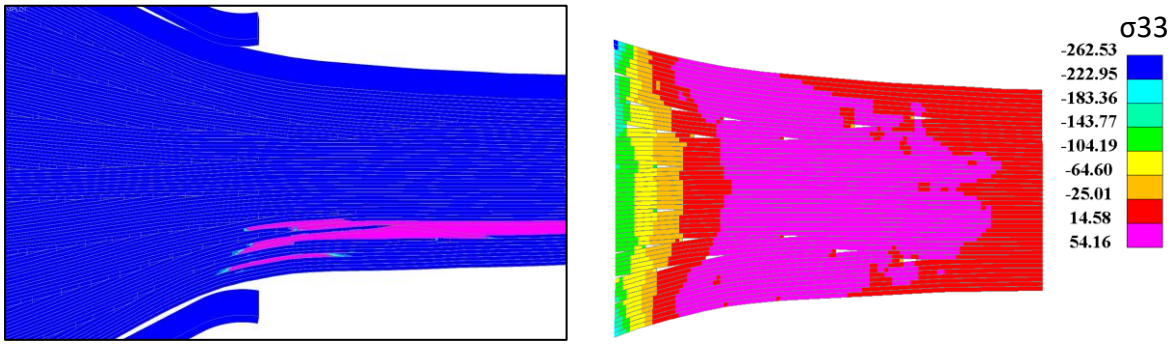


(b) (c)

Fig. 10. (a) The initial edge delamination with inset contour plot of mode ratio, (b) the catastrophic delaminations around ply drops 1, 2 and 3 and (c) the through-thickness normal stress contour of plies at 98.5% of the predicted delamination load, given by the severely tapered FE model when using the baseline cohesive propertie in Table 2 (unit: MPa).

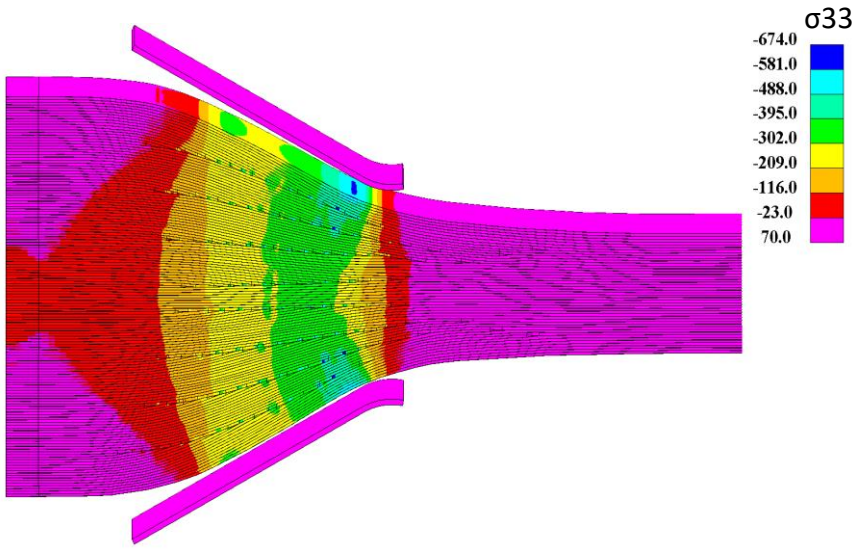


Fig. 11. FE predicted through-thickness compressive stress fields of interlaminar interfaces at 99.0% of the predicted peak load due to delamination (unit: MPa).

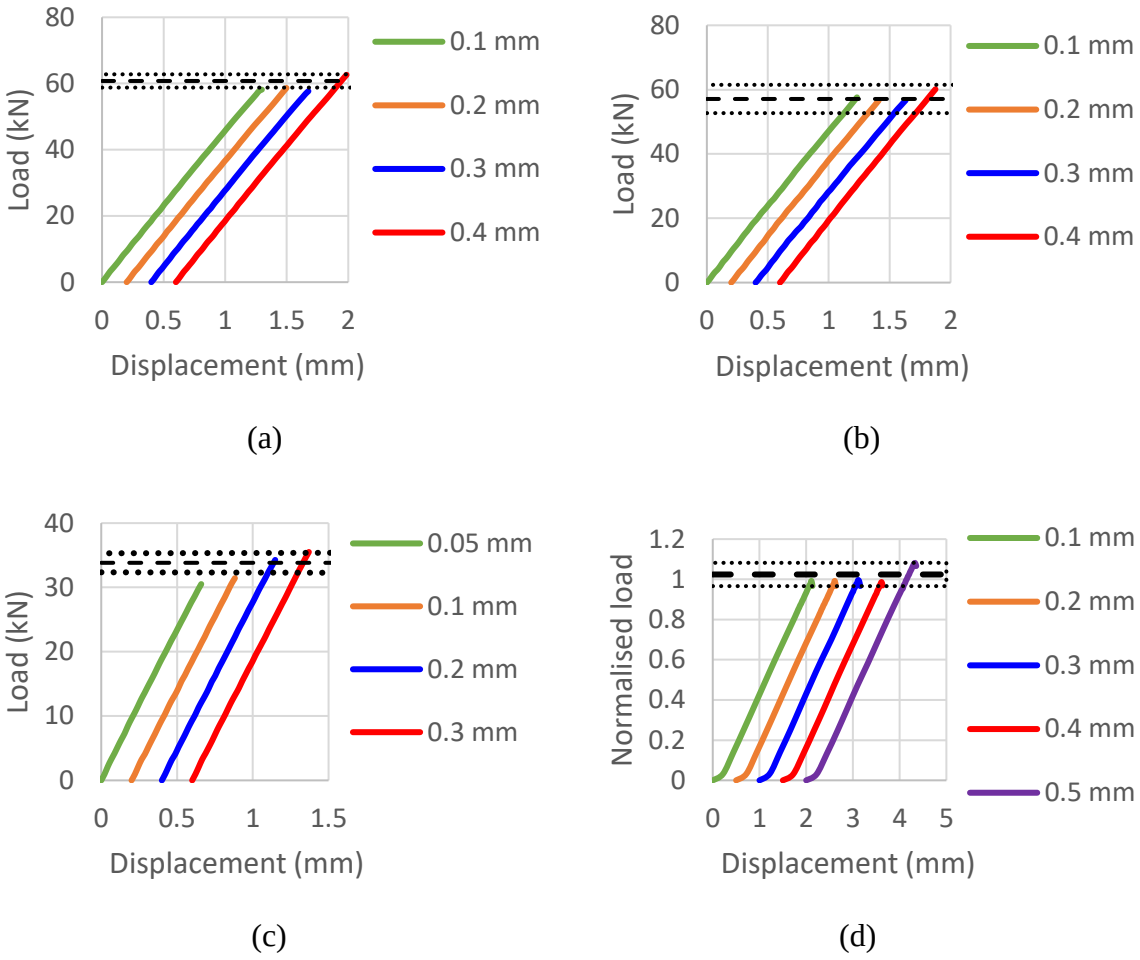


Fig. 12. Effects of element length for (a) the 8.1° laminate, (b) the 11.3° laminate, (c) the 8.1° laminate with artificial defect and (d) the severely tapered laminate; dashed black lines indicate the experimental average and bounds of the peak loads due to delamination.

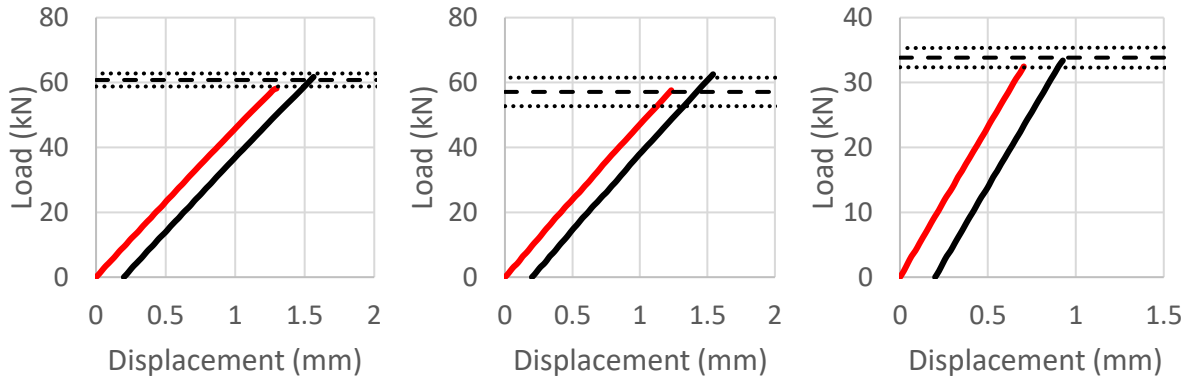


Fig. 13. Effects of cohesive strength pair for (a) the 8.1° laminate, (b) the 11.3° laminate and (c) the 8.1° defect laminate; red lines correspond to the cohesive strength pair of [60 MPa, 90 MPa]; black lines correspond to [90 MPa, 110 MPa]; dashed black lines indicate the experimental average and bounds of the peak loads due to delamination.

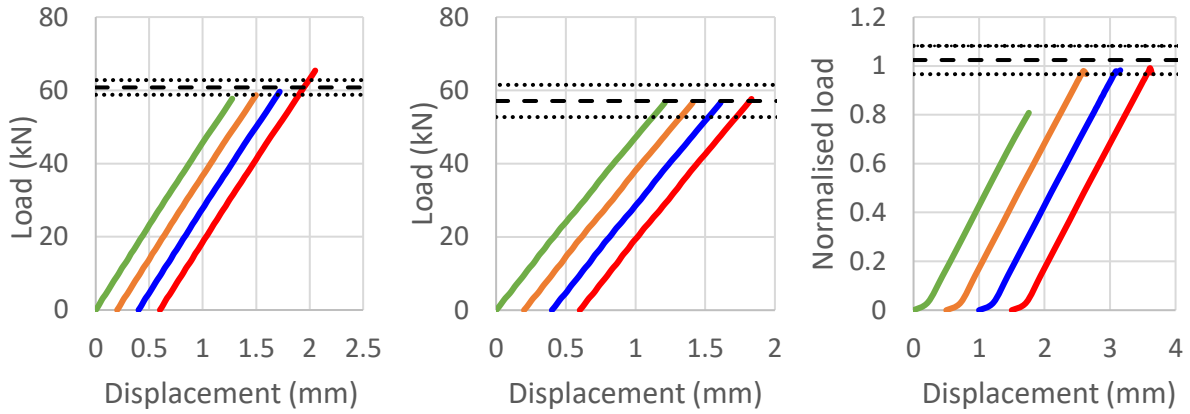


Fig. 14. Effects of TTC enhancement definition for (a) the 8.1° laminate, (b) the 11.3° laminate and (c) the severely tapered laminate; green lines correspond to Law C with 0.3 enhancement factor; orange lines correspond to Law C with 0.5 enhancement factor; blue lines correspond to Law C with 0.74 enhancement factor; red lines correspond to Law A with the enhancement factor pair of [0.3, 0.064]; dashed black lines indicate the experimental average and bounds of the peak loads due to delamination.

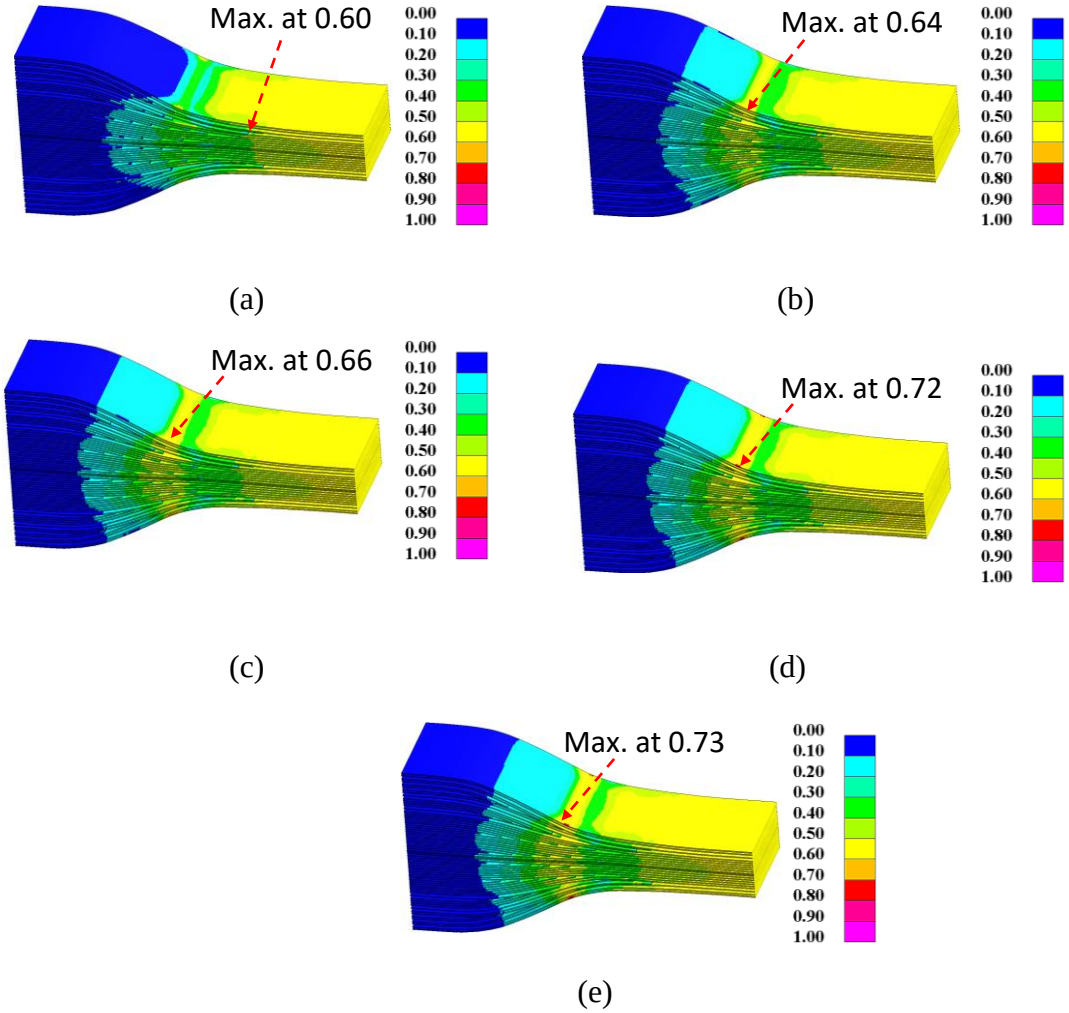


Fig. 15. Fibre damage variable fields in the 0° plies of the severely tapered laminate, predicted by the fibre failure criterion defined by Eq. 10 with (a) $\alpha=\beta=\gamma=\delta=0$, (b) $\alpha=1$ and $\beta=\gamma=\delta=0$, (c) $\alpha=\beta=1$ and $\gamma=\delta=0$, (d) $\alpha=\beta=\gamma=1$ and $\delta=0$, and (e) $\alpha=\beta=\gamma=\delta=1$.